AIAA JOURNAL
Vol. 49, No. 10, October 2011

Mixed Piezothermoelastic Finite Element Model for THUNDER Actuators

Xiaobing Wang*
Beijing Municipal Institute of Labour Protection, 100054 Beijing, People's Republic of China
Yinghua Liu†
Tsinghua University, 100084 Beijing, People's Republic of China
Wei Gao‡
University of New South Wales, Sydney, New South Wales 2052, Australia
and
Jianjun Chen§
Xidian University, 710071 Shaanxi, People's Republic of China

DOI: 10.2514/1.J050284

This paper presents a mixed piezothermoelastic finite element model for a special THUNDER (thin-layer unimorph ferroelectric driver) actuator's structures. In the mixed piezothermoelastic model, an element includes four displacement nodes, eight temperature nodes, and two potential nodes. Dynamic analyses are implemented to investigate the thermal deformation during the cooling process, deflection caused by the repolarization in the repoling process, and the piezothermoelastic coupling effect in the actuating process. The relationships between these three types of dynamic behaviors are developed by using their initial displacements. Numerical examples are given to demonstrate the proposed model and method. The accuracy of the computational results obtained by using the mixed piezothermoelastic model is sufficient. The THUNDER actuator has good properties on both actuating deflection and resisting load. In engineering applications, thermal strains have a significant effect on dome height, although thermoelectric coupling is relative small but still noticeable. Numerical results show that piezothermoelastic dynamic analysis is necessary for a THUNDER actuator to be used more effectively and accurately.

Nomenclature

A	=	area of single surface of the whole PZT layer
a, b, c	=	lengths of a element in the directions of x, y, and z
$\boldsymbol{B}$	=	strain matrix
$\boldsymbol{B}_u^0$	=	initial strain matrix
C	=	specific heat capacity
C_V	=	capacitance
D_z	=	electric displacement
d_{31}, d_{31}	=	piezoelectric strain constants
E	=	electric field intensity
$\boldsymbol{e}$	=	matrix of piezoelectric coefficients
$\boldsymbol{F}$	=	force vector (mechanical or heat)
$\boldsymbol{f}$	=	surface force on a unit surface
h_v	=	thermal convection coefficient
$\boldsymbol{K}$	=	stiffness matrix
k	=	thermal conductivity coefficient
$\boldsymbol{M}$	=	mass matrix
$\boldsymbol{P}_b$	=	body force in a unit volume
P_3	=	pyroelectric constant
$\bar{Q}$	=	surface charge on a unit surface
$\boldsymbol{q}$	=	vector of displacement
q_{heat}	=	heat flux
$\boldsymbol{q}_i$	=	vector of displacement of ith node
q_{repole}	=	initial displacement vector after the repoling process is completed
q_0	=	initial displacement vector
$\boldsymbol{S}^E$	=	matrix of elastic constant
T, T_0, T_∞	=	instantaneous, initial, and environmental temperature
T_i	=	ith temperature node
t	=	thickness
$\boldsymbol{N}$	=	shape function
u, v, w	=	displacements in the directions of x, y, and z
$\boldsymbol{V}_z$	=	voltage applied
x, y, z	=	coordinates
x_0, y_0, z_0	=	coordinates of the element's geometric center point
α_v	=	scalar of constitutive coefficient
α_x, α_y	=	thermal expansion coefficients at x and y directions
γ_{xy}	=	shear strain
δ	=	variation operator
δ_D	=	Dirac function
$\varepsilon_{\text{cool}}$	=	strain vector formed in the cooling process
$\varepsilon_{\text{repole}}$	=	strain vector caused by repolarization
$\varepsilon_x, \varepsilon_y$	=	strains in the directions of x and y
$\boldsymbol{\varepsilon}_0$	=	initial displacement vector
ε_{33}^E	=	dielectric constant or permittivity
η	=	entropy density
Θ	=	temperature variation
λ_s	=	saturation electrostriction value
$\boldsymbol{\lambda}$	=	matrix of temperature stress coefficients
μ	=	Poisson ratio
ρ	=	mass density
$\boldsymbol{\sigma}$	=	stress vector
$\bar{\boldsymbol{\sigma}}$	=	surface charge on a unit surface
Φ	=	potential
Φ_A, Φ_B	=	potential nodes
$\nabla\theta$	=	gradient of temperature variation

Received 31 October 2009; revision received 3 February 2011; accepted for publication 20 February 2011.

*Assistant Researcher, State Environmental Protection Engineering Center for City Noise & Vibration Control.
†Professor, School of Aerospace, Key Laboratory for Applied Mechanics of the Ministry of Education; yhliu@mail.tsinghua.edu.cn.
‡Senior Lecturer, School of Civil and Environmental Engineering.
§Professor, School of Electronic and Mechanical Engineering.

I. Introduction

THUNDER actuator (thin-layer unimorph ferroelectric driver, developed at the NASA Langley Research Center), a type of prestressed piezoelectric actuator, has been further developed actively in the past 10 years. It has good combination property on actuating displacement and carrying load compared with traditional direct extensional flat actuators, and can be fabricated in any size and thickness [1]. As depicted in Fig. 1, a typical THUNDER actuator consists of a piezoelectric wafer, a thin sheet of aluminum, LaRC-SI[¶] adhesive layers, and a metal backing of stainless steel or brass. In an autoclave at a temperature of 325°C with a pressure of 100 psi, LaRC-SI adhesive is cured and all layers are bonded together in a flat condition. After pressure is released and the laminated plates is cooled to room temperature 25°C, internal stress and curved shape are induced due to difference in coefficients of thermal expansion of the various layers. The process is referred to as the cooling process. In the above process, the THUNDER materials are heated to temperature in the proximity of the Curie temperature, so piezoceramic wafer needs to be repoled by applying a large dc voltage on it to align dipole moments in the thickness direction, the process is referred to as the repoling process. More details concerning the cooling process and the repoling process can be found in [2,3]. When the manufacture of a THUNDER actuator is finished, an applied external voltage can induce an actuating displacement, which is referred to here as the actuating process.

For a THUNDER actuator, the internal stress and curved shape play an important role in its actuating capability, and they are mainly induced in the cooling process. In the past 10 years, the curved shape due to the cooling process and the actuating capability in the actuating process has been studied widely, in which classical lamination theory, von Kármán nonlinear plate theory, and Rayleigh–Ritz techniques were involved [2,4,5]. To study the stability and bifurcation of the shape formed in the cooling process [4], a four-term Rayleigh–Ritz technique was employed to approximate the displacement fields [6]. This was improved by a 23-term Rayleigh–Ritz model [7] and the better accuracy was verified by experiments [8]. In numerical simulations, parallel algorithm was applied to deal with the problem involving a large number of degrees of freedom generated from modeling each thin layer by solid elements [9]. In experimental investigations, the dome height formed in the cooling process and the actuating displacements were measured [2,4,5], and the actuating capability of a THUNDER actuator with various end conditions [10] or in the case of mechanical preloads [11] was investigated. The actuating capability of RAINBOW (reduced and internally biased oxide wafer) and THUNDER actuators were compared in the case of the two actuators having the same piezoelectric compositions, geometries and ceramic-to-metal thickness ratios [12]. In engineering applications, the good ability of THUNDER actuator in vibration control was exhibited in experiments [13,14], and so on.

The above research related the cooling process with the actuating process, but did not involve the repoling process, which lies in the middle of the cooling process and actuating process. Capozzoli et al. [3] especially studied the effect on dome height due to the repoling process and pointed out that the repolarization produces a subsequent reduction in curvature because of the realignment of dipole moments in the transverse direction. Based on ferroelectric domain theory, they calculated the reduction and proved that the repolarization has a significant effect on dome height through experiments [2]. Therefore, to study the evolution process of dome height or shape of a THUNDER actuator systematically, the repoling process should be considered between the cooling process and actuating process, which is one of the main works in this paper.

Temperature variation plays an important role in the internal stress and curved shape in the cooling process, and it is still an important factor in the actuating process, because the curved shape will be changed by thermal strains and pyroelectric effect. Since temperature variation is evitable for most engineering cases, it is necessary to study the piezothermoelastic coupling problem.

[¶]NASA Langley Research Center's soluble imide, a thermoplastic material developed by Dr. Robert G. Bryant.

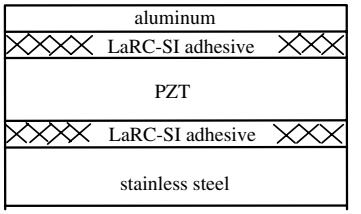

Fig. 1 Cross section of a THUNDER actuator.

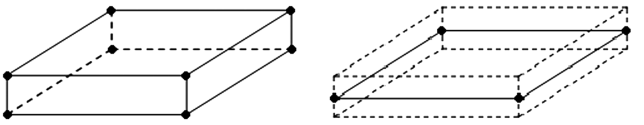

Fig. 2 Two typical piezothermoelastic element models: a) eight-node piezothermoelastic solid element model and b) four-node piezothermoelastic plate element model.

Finite element method is a powerful tool to study piezothermoelastic dynamic analysis [15]. Currently, researchers prefer defining displacement nodes, which are also considered as potential nodes and temperature nodes simultaneously, or a set of nodes that are shared by displacement nodes, potential nodes, and temperature nodes. An example is the eight-node solid element model [16–18] as depicted in Fig. 2a, in which the displacement nodes, potential nodes, and temperature nodes are all defined by the same eight nodes. The eight-node solid element model is convenient to satisfy any complex 3-D heat boundary conditions, but it is needed to introduce incompatible nodes by incorporating internal degrees of freedom to correct the excessive shear strain energy and ill-conditioned problem when the conventional isoparametric hexahedron solid element is used in a thin plate [17]. The other example is the four-node plate element model [19–22], as shown in Fig. 2b, in which the displacement nodes, potential nodes, and temperature nodes are all defined by the same four nodes located in middle plane. The four-node plate element model is convenient to describe displacement field of thin plate, but it is not easy to satisfy complicated 3-D heat boundary conditions [20]. At present, the two typical piezothermoelastic element models have already been widely used and practice shows that they are very convenient to number nodes.

Another type of model is to define displacement nodes, potential nodes, and temperature nodes independently, or each type of node is defined in its own way. This type of mixed element model has been rarely used in piezothermoelastic coupling problem, due to its inconvenience on number nodes. Since there are so many types of displacement element models, potential element models, and thermal element models to be chosen, it would be much better if they can be well combined together by using various energy principles. Then the mixed-mode element has its own advantages, such as having more freedom and multiformity in modeling for various complex structures with complicated thermal boundary conditions.

Therefore, for THUNDER actuator's special structures, a mixed piezothermoelastic finite element model is proposed in this study that combines the displacement element models, potential element models, and thermal element models. Based on the mixed model, the evolution process of dome height in the cooling process, repoling process, and actuating process is studied systematically, and the accuracy of the mixed element model and the influence of thermal strain and pyroelectric effect on actuating performance are investigated.

II. Finite Element Model

A. Mixed Piezothermoelastic Finite Element Model

Generally, a THUNDER actuator belongs to thin laminated plates, and a four-node plane displacement element model is convenient to

describe its geometric nonlinear displacement field. In view of five layers and four materials involved, an eight-node solid element model can be chosen to describe each layer's temperature field, which is easy to satisfy the complicated 3-D heat boundary conditions. Considering the top and bottom surfaces of the piezoelectric material are all coated with an electrode, such as silver epoxy [12], a two-node linear element is concise to describe its potential field. Integrating them together, a mixed piezothermoelastic finite element model is presented in Fig. 3, in which the cuboid of T_1-T_2-T_3-T_4-T_5-T_6-T_7-T_8 is the element whose size is $2a \times 2b \times 2c$; the rectangular q_i-q_j-q_m-q_p is the element's projection on the actuator's geometrical middle plane; q_i, q_j, q_m, and q_p are displacement nodes; T_1, T_2, T_3, T_4, T_5, T_6, T_7, and T_8 are temperature nodes; and Φ_A and Φ_B are potential nodes. The local coordinate system of the element is $oxyz$, whose origin is at the geometric center of the rectangular q_i-q_j-q_m-q_p. For nonpiezoelectric material layers, the element model is the remaining after potential nodes are eliminated from Fig. 3.

Considering geometric nonlinearity, the von Kármán nonlinear theory is used here [4]:

$$\begin{cases} \varepsilon_x = \frac{\partial u_0}{\partial x} + \frac{1}{2}\left(\frac{\partial \omega_0}{\partial x}\right)^2 - z\frac{\partial^2 \omega_0}{\partial x^2} \\ \varepsilon_y = \frac{\partial v_0}{\partial y} + \frac{1}{2}\left(\frac{\partial \omega_0}{\partial y}\right)^2 - z\frac{\partial^2 \omega_0}{\partial y^2} \\ \gamma_{xy} = \frac{\partial u_0}{\partial y} + \frac{\partial v_0}{\partial x} + \frac{\partial \omega_0}{\partial x}\frac{\partial \omega_0}{\partial y} - 2z\frac{\partial^2 \omega_0}{\partial x \partial y} \end{cases} \tag{1}$$

where the subscript 0 denotes the position in the actuator's geometrical middle plane.

The displacement field is defined as follows by a rectangular flat shell finite element:

$$\boldsymbol{q} = \boldsymbol{N}\boldsymbol{q}^e \tag{2}$$

where

$$\boldsymbol{q} = [\,u \quad v \quad \omega \quad \theta_x \quad \theta_y\,]^T, \qquad \boldsymbol{q}^e = [\,q_i \quad q_j \quad q_m \quad q_p\,]^T$$

$$\boldsymbol{N} = [\,N_i \quad N_j \quad N_m \quad N_p\,]$$

$$\boldsymbol{N}_k = \begin{bmatrix} N_{pk} & 0 & -z\frac{\partial N_{bk}}{\partial x} & -z\frac{\partial N_{bxk}}{\partial x} & -z\frac{\partial N_{byk}}{\partial x} \\ 0 & N_{pk} & -z\frac{\partial N_{bk}}{\partial y} & -z\frac{\partial N_{bxk}}{\partial y} & -z\frac{\partial N_{byk}}{\partial y} \\ 0 & 0 & N_{bk} & N_{bxk} & N_{byk} \\ 0 & 0 & \partial N_{bk}/\partial y & \partial N_{bxk}/\partial y & \partial N_{byk}/\partial y \\ 0 & 0 & -\partial N_{bk}/\partial x & -\partial N_{bxk}/\partial x & -\partial N_{byk}/\partial x \end{bmatrix}$$

$$k = i, j, m, p \tag{3}$$

where N_{pk}, N_{bk}, N_{bxk}, and N_{byk} are corresponding interpolation functions.

Substituting Eq. (2) into Eq. (1) yields

$$\boldsymbol{\varepsilon} = \boldsymbol{B}_u \boldsymbol{q}^e = (\boldsymbol{B}_L + \boldsymbol{B}_{\text{non}})\boldsymbol{q}^e \tag{4}$$

where

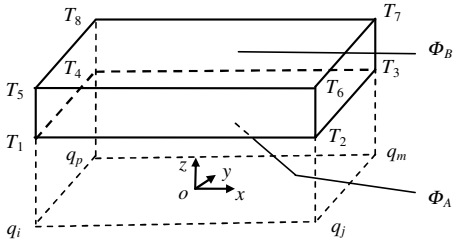

Fig. 3 Mixed piezothermoelastic element model.

$$\boldsymbol{\varepsilon} = [\,\varepsilon_x \quad \varepsilon_y \quad \gamma_{xy}\,]^T, \qquad \boldsymbol{B}_L = [\,\boldsymbol{B}_{Li} \quad \boldsymbol{B}_{Lj} \quad \boldsymbol{B}_{Lm} \quad \boldsymbol{B}_{Lp}\,]$$

$$\boldsymbol{B}_{\text{non}} = \left[\,\tfrac{1}{2}\boldsymbol{L}_x \boldsymbol{q}^e \boldsymbol{L}_x \quad \tfrac{1}{2}\boldsymbol{L}_y \boldsymbol{q}^e \boldsymbol{L}_y \quad \boldsymbol{L}_x \boldsymbol{q}^e \boldsymbol{L}_y\,\right]^T$$

$$\boldsymbol{B}_{Lk} = \begin{bmatrix} \frac{\partial N_{pk}}{\partial x} & 0 & -z\frac{\partial^2 N_{bk}}{\partial x^2} & -z\frac{\partial^2 N_{bxk}}{\partial x^2} & -z\frac{\partial^2 N_{byk}}{\partial x^2} \\ 0 & \frac{\partial N_{pk}}{\partial y} & -z\frac{\partial^2 N_{bk}}{\partial y^2} & -z\frac{\partial^2 N_{bxk}}{\partial y^2} & -z\frac{\partial^2 N_{byk}}{\partial y^2} \\ \frac{\partial N_{pk}}{\partial y} & \frac{\partial N_{pk}}{\partial x} & -2z\frac{\partial^2 N_{bk}}{\partial x \partial y} & -2z\frac{\partial^2 N_{bxk}}{\partial x \partial y} & -2z\frac{\partial^2 N_{byk}}{\partial x \partial y} \end{bmatrix}$$

$$(k = i, j, m, p)$$

$$\boldsymbol{L}_x = [\boldsymbol{L}_{xi} \quad \boldsymbol{L}_{xj} \quad \boldsymbol{L}_{xm} \quad \boldsymbol{L}_{xp}], \quad \boldsymbol{L}_y = [\boldsymbol{L}_{yi} \quad \boldsymbol{L}_{yj} \quad \boldsymbol{L}_{ym} \quad \boldsymbol{L}_{yp}]$$

$$\boldsymbol{L}_{xk} = \left[0 \;\; 0 \;\; \frac{\partial N_{bk}}{\partial x} \;\; \frac{\partial N_{bxk}}{\partial x} \;\; \frac{\partial N_{byk}}{\partial x}\right], \quad \boldsymbol{L}_{yk} = \left[0 \;\; 0 \;\; \frac{\partial N_{bk}}{\partial y} \;\; \frac{\partial N_{bxk}}{\partial y} \;\; \frac{\partial N_{byk}}{\partial y}\right] \tag{5}$$

The electrical potential field is defined as follows using linear interpolation:

$$\Phi = \boldsymbol{N}_{\boldsymbol{\Phi}} \boldsymbol{\Phi}^e \tag{6}$$

where

$$\boldsymbol{\Phi}^e = [\,\Phi_A \quad \Phi_B\,]^T, \qquad \boldsymbol{N}_{\boldsymbol{\Phi}} = \frac{1}{t_{\text{PZT}}}[\,z - z_{\text{PZT}_B} \quad z_{\text{PZT}_A} - z\,] \tag{7}$$

where z_{PZT_A} and z_{PZT_B} are the z coordinate values of the PZT layer's top and bottom surfaces, respectively.

The positive direction of electric field is defined as the same as the z axis, then the electric field intensity at the z direction can be expressed as

$$E_z = -\boldsymbol{B}_{\boldsymbol{\Phi}} \boldsymbol{\Phi}^e, \qquad \boldsymbol{B}_{\boldsymbol{\Phi}} = \frac{1}{t_{\text{PZT}}}[\,1 \quad -1\,] \tag{8}$$

Temperature variation of any point in an element is defined as

$$\theta = \boldsymbol{N}_\theta \boldsymbol{\theta}^e \tag{9}$$

where $\theta = T - T_0$, T and T_0 are the instantaneous and initial temperatures, respectively, and

$$\boldsymbol{\theta}^e = [\,\theta_a \quad \theta_b \quad \theta_c \quad \theta_d \quad \theta_e \quad \theta_f \quad \theta_g \quad \theta_h\,]^T$$

$$\boldsymbol{N}_\theta = [\,N_{\theta a} \quad N_{\theta b} \quad N_{\theta c} \quad N_{\theta d} \quad N_{\theta e} \quad N_{\theta f} \quad N_{\theta g} \quad N_{\theta h}\,]$$

$$N_{\theta k} = (1 + \xi_k \xi)(1 + \eta_k \eta)(1 + \zeta_k \zeta)/8, \qquad k = a, b, \ldots, g \tag{10}$$

where $\xi = (x - x_0)/a$, $\eta = (y - y_0)/b$, and $\zeta = (z - z_0)/c$ and x_0, y_0, and z_0 are the element's geometric center coordinates.

Then the gradient of temperature variation can be solved as

$$\nabla\theta = -\boldsymbol{B}_\theta \boldsymbol{\theta}^e \tag{11}$$

where

$$\boldsymbol{B}_\theta = -[\,\partial \boldsymbol{N}_\theta^T/\partial x \quad \partial \boldsymbol{N}_\theta^T/\partial y \quad \partial \boldsymbol{N}_\theta^T/\partial z\,]^T \tag{12}$$

B. Constitutive Relations

For a THUNDER actuator, its piezoelectric material is often polarized in the thickness direction or z direction only, and then the piezothermoelastic constitutive relations of piezoelectric material can be simplified as [17]

$$\boldsymbol{\sigma} = \boldsymbol{S}^E(\boldsymbol{\varepsilon} - \boldsymbol{\varepsilon}_0) - \boldsymbol{e}E_z - \boldsymbol{\lambda}\theta \tag{13}$$

$$D_z = \boldsymbol{e}^T(\boldsymbol{\varepsilon} - \boldsymbol{\varepsilon}_0) + \varepsilon_{33}^E E_z + P_3\theta \tag{14}$$

$$\eta = \boldsymbol{\lambda}^T(\boldsymbol{\varepsilon} - \boldsymbol{\varepsilon}_0) + P_3 E_z + \alpha_v \theta \tag{15}$$

where $\boldsymbol{\sigma}$ is the stress vector; $\boldsymbol{\varepsilon}_0$ is the initial displacement vector; $\boldsymbol{S}^E$ is the matrix of elastic constant; $\boldsymbol{e} = (\boldsymbol{S}^E)^T(\,d_{31} \quad d_{32} \quad 0\,)^T$ is the matrix of piezoelectric coefficients; d_{31} and d_{32} are the piezoelectric strain constants along the x and y directions, respectively, when the direction of electric field applied is the z direction; $\boldsymbol{\lambda} = \boldsymbol{S}^{\boldsymbol{E}}(\,\alpha_x \quad \alpha_y \quad 0\,)^T$ is the matrix of temperature stress coefficients; α_x and α_y are thermal expansion coefficients at x and y directions, respectively; D_z is electric displacement; ε_{33}^E is the dielectric constant or permittivity; P_3 is the pyroelectric constant; η is entropy density; $\alpha_v = \rho C/T_0$ is the scalar of constitutive coefficient; C is specific heat capacity; and ρ is mass density.

C. Finite Element Equations

For piezothermoelastic coupling problem, the following three equations can be derived from the principle of virtual work [17,23]:

$$\int_V \delta\boldsymbol{\varepsilon}^T\boldsymbol{\sigma}\,\mathrm{d}V = \delta\boldsymbol{q}^T\boldsymbol{F} + \int_S \delta\boldsymbol{q}^T\boldsymbol{f}\,\mathrm{d}S + \int_V \delta\boldsymbol{q}^T(\boldsymbol{P}_b - \rho\ddot{\boldsymbol{q}})\,\mathrm{d}V \tag{16}$$

$$\int_{V_{\mathrm{PZT}}} \delta\boldsymbol{E}^T\boldsymbol{D}\,\mathrm{d}V = \int_{S_{\mathrm{PZT}}} \delta\boldsymbol{\Phi}^T\bar{Q}\,\mathrm{d}S \tag{17}$$

$$T_0\int_V \delta\boldsymbol{\theta}^T\dot{\boldsymbol{\eta}}\,\mathrm{d}V = -\int_V \delta(\nabla\boldsymbol{\theta})k(\nabla\boldsymbol{\theta})\,\mathrm{d}V + \int_S \delta\boldsymbol{\theta}^T\boldsymbol{q}_{\mathrm{heat}}\,\mathrm{d}S - \int_S \delta\boldsymbol{\theta}^T h_v(\theta + T_0 - T_\infty)\,\mathrm{d}S \tag{18}$$

where δ is the variation operator, $\boldsymbol{F}$ is the vector of concentrated force, $\boldsymbol{f}$ is surface force on a unit surface, $\boldsymbol{P}_b$ is body force in a unit volume, $\bar{Q}$ is the surface charge on a unit surface, k is thermal conductivity coefficient, $\boldsymbol{q}_{\mathrm{heat}}$ is heat flux, h_v is thermal convection coefficient, and T_∞ is environmental temperature.

The capacitance C_V for the piezoelectric wafer having conductive electrodes on the top and bottom surfaces can be expressed as

$$C_V = \varepsilon_{33}^E A/t_{\mathrm{PZT}} \tag{19}$$

where A is the area of a single surface of the whole PZT layer.

When voltage $\boldsymbol{V}_z$ is applied on the piezoelectric wafer in the thickness direction, according to the relationship among electric charge, voltage, and capacitance, the surface charge on a unit surface $\bar{\boldsymbol{\sigma}}$ can be obtained as

$$\bar{Q} = \varepsilon_{33}^E V_z/t_{\mathrm{PZT}} \tag{20}$$

Now all components in Eqs. (16–18) are known. Substituting all components into Eqs. (16–18) and considering the arbitrariness of $\delta\boldsymbol{q}$, $\delta\boldsymbol{\Phi}$ and $\delta\boldsymbol{\theta}$, the piezothermoelastic finite element equations can be finally obtained as

$$\boldsymbol{M}_{uu}\ddot{\boldsymbol{q}} + \boldsymbol{K}_{uu}\boldsymbol{q} + \boldsymbol{K}_{u\Phi}\boldsymbol{\Phi} - \boldsymbol{K}_{u\theta}\boldsymbol{\theta} = \boldsymbol{K}_{uu}^{t0}\boldsymbol{q}_0 + \boldsymbol{F} + \boldsymbol{F}_f + \boldsymbol{F}_{p_b} \tag{21}$$

$$-\boldsymbol{K}_{\Phi u}\boldsymbol{q} + \boldsymbol{K}_{\Phi\Phi}\boldsymbol{\Phi} - \boldsymbol{K}_{\Phi\theta}\boldsymbol{\theta} = \boldsymbol{F}_\Phi - \boldsymbol{K}_{\Phi u}^{t0}\boldsymbol{q}_0 \tag{22}$$

$$C_{\theta u1}\dot{\boldsymbol{q}} + C_{\theta u2}\boldsymbol{q} - \boldsymbol{C}_{\theta\Phi}\dot{\boldsymbol{\Phi}} + \boldsymbol{C}_{\theta\theta}\dot{\boldsymbol{\theta}} + (\boldsymbol{K}_{\theta\theta} + \boldsymbol{K}_{\theta\theta_h})\boldsymbol{\theta} = \boldsymbol{F}_{\theta_c} + \boldsymbol{F}_{\theta_h} \tag{23}$$

where symbols are given in the Appendix.

III. Discussion

Equations (21–23) are only general piezothermoelastic finite element equations for a THUNDER actuator. In fact, for the three stages corresponding to the cooling process, repoling process, and actuating process, a THUNDER actuator has different physical properties, and the corresponding dynamic equations are different. They are discussed one by one as follows.

A. Cooling Process

In the cooling process, a THUNDER actuator is heated to approach the Curie temperature approximately and its piezoelectric wafer loses a great deal of polarization, the piezoelectric material almost acts as a normal dielectric [3]. Then electromechanical coupling problem can be neglected in the cooling process and the static equation of heat deformation with zero initial displacements is expressed as

$$\boldsymbol{K}_{uu}\boldsymbol{q} = \boldsymbol{K}_{u\theta}\boldsymbol{\theta} \tag{24}$$

Because $\boldsymbol{K}_{uu}$ and $\boldsymbol{K}_{u\theta}$ are functions of $\boldsymbol{q}$, Eq. (24) is a nonlinear algebraic equation and can be solved by using quasi-Newton method and Broyden–Fletcher–Goldfarb–Shanno method:

$$\boldsymbol{q}^{(n+1)} = \boldsymbol{q}^{(n)} - (\boldsymbol{K}_T^{(n)})^{-1}\Gamma^{(n)} \tag{25}$$

where

$$\Gamma^{(n)} = \boldsymbol{K}_{uu}\boldsymbol{q} - \boldsymbol{K}_{u\theta}\boldsymbol{\theta}$$

$$(\boldsymbol{K}_T^{(n+1)})^{-1} = \left(\boldsymbol{I} - \frac{\Delta\boldsymbol{q}^{(n)}(\Delta\Gamma^{(n)})^T}{(\Delta\boldsymbol{q}^{(n)})^T\Delta\Gamma^{(n)}}\right)(\boldsymbol{K}_T^{(n)})^{-1}\left(\boldsymbol{I} - \frac{\Delta\Gamma^{(n)}(\Delta\boldsymbol{q}^{(n)})^T}{(\Delta\boldsymbol{q}^{(n)})^T\Delta\Gamma^{(n)}}\right) + \frac{\Delta\boldsymbol{q}^{(n)}(\Delta\boldsymbol{q}^{(n)})^T}{(\Delta\boldsymbol{q}^{(n)})^T\Delta\Gamma^{(n)}} \tag{26}$$

From Eqs. (21–23), the dynamic equations of the cooling process can be developed as

$$\boldsymbol{M}_{uu}\ddot{\boldsymbol{q}} + \boldsymbol{K}_{uu}\boldsymbol{q} - \boldsymbol{K}_{u\theta}\boldsymbol{\theta} = \boldsymbol{F} + \boldsymbol{F}_f + \boldsymbol{F}_{p_b} \tag{27}$$

$$C_{\theta u1}\dot{\boldsymbol{q}} + C_{\theta u2}\boldsymbol{q} + \boldsymbol{C}_{\theta\theta}\dot{\boldsymbol{\theta}} + (\boldsymbol{K}_{\theta\theta} + \boldsymbol{K}_{\theta\theta_h})\boldsymbol{\theta} = \boldsymbol{F}_{\theta_c} + \boldsymbol{F}_{\theta_h} \tag{28}$$

B. Repoling Process

To align dipole moments in the thickness direction, the next manufacturing process is to apply a large dc voltage on the piezoelectric material. The strain $\boldsymbol{\varepsilon}_{\mathrm{repole}}$ induced by repolarization has been studied by Capozzoli et al. [3]. Based on their work and considering the initial strain formed in the cooling process, the constitutive relationship in the repoling process with constant temperature can be obtained as

$$\boldsymbol{\sigma} = \boldsymbol{S}^E(\boldsymbol{\varepsilon} - \boldsymbol{\varepsilon}_{\mathrm{cool}} + \delta_D\boldsymbol{\varepsilon}_{\mathrm{repole}}) \tag{29}$$

where

$$\boldsymbol{\varepsilon}_{\mathrm{repole}} = \left[\tfrac{3}{2}\mu\lambda_s \quad \tfrac{3}{2}\mu\lambda_s \quad 0\right]^T \tag{30a}$$

$$\delta_D = \begin{cases} 0 & \text{piezoelectric material layer} \\ 1 & \text{other layers} \end{cases} \tag{30b}$$

$\boldsymbol{\varepsilon}_{\mathrm{cool}}$ is the strain vector formed in the cooling process, $\boldsymbol{\varepsilon}_{\mathrm{repole}}$ is the strain vector caused by repolarization, μ is the Poisson ratio, and λ_s is the saturation electrostriction value.

According to Eqs. (16) and (29), the dynamic equation of the repoling process is given by

$$\boldsymbol{M}_{uu}\ddot{\boldsymbol{q}} + \boldsymbol{K}_{uu}\boldsymbol{q} = \boldsymbol{F}_0 - \boldsymbol{F}_{\mathrm{repole}} \tag{31}$$

where

$$\boldsymbol{F}_0 = \int_{V_{\mathrm{AL}}+V_{\mathrm{SI}_1}+V_{\mathrm{PZT}}+V_{\mathrm{SI}_2}+V_{\mathrm{steel}}} \boldsymbol{B}_u^T\boldsymbol{S}^E\boldsymbol{\varepsilon}_{\mathrm{cool}}\,\mathrm{d}V$$

$$F_{\mathrm{repole}} = \int_{V_{\mathrm{PZT}}} \boldsymbol{B}_u^T\boldsymbol{S}^E\boldsymbol{\varepsilon}_{\mathrm{repole}}\,\mathrm{d}V \tag{32}$$

Table 1 Material properties for dome-height verification [2,3,5,22,24]

Property	PZT 5A	Stainless steel	Aluminum	LaRC-SI adhesive
Thickness t, mm	0.1727	0.0762	0.0254	0.0254
Young's modulus E, GPa	62.055	262.010	68.950	3.999
Poisson's ratio μ	0.31	0.33	0.33	0.45
Thermal expansion α, $1/^\circ$C	1.5	17.3	24	46
Density ρ, kg/m^3	7750	7750	2787	1376
Thermal conduction k, W m^{-1} °C^{-1}	1.5	35	104	0.244
Heat capacitance C, J kg^{-1} °C^{-1}	420	465	883	1.2
Piezoelectric constant d_{31}, 10^{-12} m/V	−170.18	——	——	——
Electric permittivity ε_{33}, 10^{-9} F/m	15.039	——	——	——
Pyroelectric constant p_3, 10^{-3} C m^{-2}°C^{-1}	−0.2	——	——	——
Saturation electrostriction value λ_s	1.11×10^{-3}	——	——	——

C. Actuating Process Without Temperature Variation

After the repoling process is completed, a THUNDER actuator can be used as an actuator or sensor, and then its static electromechanical coupling equations at room temperature can be derived as follows from Eqs. (21–23):

$$\boldsymbol{K}_{uu}\boldsymbol{q} + \boldsymbol{K}_{u\Phi}\boldsymbol{\Phi} = \boldsymbol{K}_{uu}^{t0}\boldsymbol{q}_0 + \boldsymbol{F} + \boldsymbol{F}_f + \boldsymbol{F}_{p_b} \tag{33}$$

$$-\boldsymbol{K}_{\Phi u}\boldsymbol{q} + \boldsymbol{K}_{\Phi\Phi}\boldsymbol{\Phi} = \boldsymbol{F}_{\boldsymbol{\Phi}} - \boldsymbol{K}_{\Phi u}^{t0}\boldsymbol{q}_0 \tag{34}$$

where

$$\boldsymbol{q}_0 = \boldsymbol{q}_{\text{repole}}, \qquad \boldsymbol{B}_u^0 = (\boldsymbol{B}_L + \boldsymbol{B}_{\text{non}})_{\boldsymbol{q}_0=\boldsymbol{q}_{\text{repole}}} \tag{35}$$

where $\boldsymbol{q}_{\text{repole}}$ is initial displacement vector after the repoling process finished.

Substituting Eq. (34) into Eq. (33) yields

$$\boldsymbol{M}_{uu}\ddot{\boldsymbol{q}} + (\boldsymbol{K}_{uu} + \boldsymbol{K}_{u\Phi}\boldsymbol{K}_{\Phi\Phi}^{-1}\boldsymbol{K}_{\Phi u})\boldsymbol{q} = \boldsymbol{K}_{uu}^{t0}\boldsymbol{q}_0 + \boldsymbol{K}_{u\Phi}\boldsymbol{K}_{\Phi\Phi}^{-1}\boldsymbol{K}_{\Phi u}^{t0}\boldsymbol{q}_0 + \boldsymbol{F} + \boldsymbol{F}_f + \boldsymbol{F}_{p_b} - \boldsymbol{K}_{u\Phi}\boldsymbol{K}_{\Phi\Phi}^{-1}\boldsymbol{F}_{\boldsymbol{\Phi}} \tag{36}$$

Comparing Eq. (36) with Eq. (31), it can be seen that the stiffness matrix changes from $\boldsymbol{K}_{uu}$ to $\boldsymbol{K}_{uu} + \boldsymbol{K}_{u\Phi}\boldsymbol{K}_{\Phi\Phi}^{-1}\boldsymbol{K}_{\Phi u}$. At the same time, an additional force $\boldsymbol{K}_{u\Phi}\boldsymbol{K}_{\Phi\Phi}^{-1}\boldsymbol{K}_{\Phi u}^{t0}\boldsymbol{q}_0$ emerges in the right side of Eq. (36) due to the resumption of piezoelectric property after repolarization.

D. Actuating Process with Temperature Variation

When temperature is changed in engineering application, the piezothermoelastic dynamic equations of a THUNDER actuator are presented as Eqs. (21–23), in which initial displacement vector $\boldsymbol{q}_0$ and initial strain matrix $\boldsymbol{B}_u^0$ can be obtained from Eq. (35).

Equations (21–23) are equivalent to the following equation in state space:

$$\boldsymbol{A}\dot{\boldsymbol{x}} = \boldsymbol{B}\boldsymbol{x} + \boldsymbol{u} \tag{37}$$

where

$$\boldsymbol{x} = [\boldsymbol{q} \quad \dot{\boldsymbol{q}} \quad \boldsymbol{\theta}]^T, \qquad \boldsymbol{A} = \begin{bmatrix} \boldsymbol{I} & \boldsymbol{0} & \boldsymbol{0} \\ \boldsymbol{0} & \boldsymbol{M}_{uu} & \boldsymbol{0} \\ \boldsymbol{0} & \boldsymbol{0} & \boldsymbol{e}_L \end{bmatrix}$$

$$\boldsymbol{B} = \begin{bmatrix} \boldsymbol{0} & \boldsymbol{I} & \boldsymbol{0} \\ -\boldsymbol{a}_L(\boldsymbol{q}) & \boldsymbol{0} & -\boldsymbol{b}_L(\boldsymbol{q}) \\ -\boldsymbol{w}_L(\boldsymbol{q}) & -\boldsymbol{d}_L(\boldsymbol{q}) & -\boldsymbol{f}_L \end{bmatrix}, \qquad \boldsymbol{u} = \begin{Bmatrix} \boldsymbol{0} \\ \boldsymbol{c}_L(\boldsymbol{q}) \\ \boldsymbol{g}_L \end{Bmatrix}$$

$$\boldsymbol{a}_L(\boldsymbol{q}) = \boldsymbol{K}_{uu}(\boldsymbol{q}) + \boldsymbol{K}_{u\Phi}(\boldsymbol{q})\boldsymbol{K}_{\Phi\Phi}^{-1}\boldsymbol{K}_{\Phi u}(\boldsymbol{q})$$

$$\boldsymbol{b}_L(\boldsymbol{q}) = \boldsymbol{K}_{u\Phi}(\boldsymbol{q})\boldsymbol{K}_{\Phi\Phi}^{-1}\boldsymbol{K}_{\Phi\theta} - \boldsymbol{K}_{u\theta}(\boldsymbol{q})$$

$$\boldsymbol{c}_L(\boldsymbol{q}) = (\boldsymbol{K}_{uu}^{t0}(\boldsymbol{q}) + \boldsymbol{K}_{u\Phi}(\boldsymbol{q})\boldsymbol{K}_{\Phi\Phi}^{-1}\boldsymbol{K}_{\Phi u}^{t0}(\boldsymbol{q}))\boldsymbol{q}_0 + \boldsymbol{F} + \boldsymbol{F}_f + \boldsymbol{F}_{p_b} - \boldsymbol{K}_{u\Phi}(\boldsymbol{q})\boldsymbol{K}_{\Phi\Phi}^{-1}\boldsymbol{F}_{\boldsymbol{\Phi}},$$

$$\boldsymbol{d}_L(\boldsymbol{q}) = \boldsymbol{C}_{\theta u1}(\boldsymbol{q}) - \boldsymbol{C}_{\theta\Phi}\boldsymbol{K}_{\Phi\Phi}^{-1}\boldsymbol{K}_{\Phi u}(\boldsymbol{q}), \qquad \boldsymbol{e}_L = \boldsymbol{C}_{\theta\theta} - \boldsymbol{C}_{\theta\Phi}\boldsymbol{K}_{\Phi\Phi}^{-1}\boldsymbol{K}_{\Phi\theta}$$

$$\boldsymbol{f}_L = \boldsymbol{K}_{\theta\theta} + \boldsymbol{K}_{\theta\theta_h}, \qquad \boldsymbol{g}_L = \boldsymbol{C}_{\theta\Phi}\boldsymbol{K}_{\Phi\Phi}^{-1}\dot{\boldsymbol{F}}_{\boldsymbol{\Phi}} + \boldsymbol{F}_{\theta_c} + \boldsymbol{F}_{\theta_h}$$

$$\boldsymbol{w}_L = \boldsymbol{C}_{\theta u2} - \boldsymbol{C}_{\theta\Phi}\boldsymbol{K}_{\Phi\Phi}^{-1}\dot{\boldsymbol{K}}_{\Phi u}(\boldsymbol{q}) \tag{38}$$

Equation (37) is a first-order nonlinear differential equation and is not difficult to solve.

IV. Numerical Examples

For the three stages of cooling, repoling, and actuating processes, most of the work focused on one or two stages, and only static analysis or experimental investigations have been widely addressed. To the authors' knowledge, there has been very little research involving all three processes, and the piezothermoelastic coupling dynamic behavior was rarely taken into account. Here, some typical examples are studied to exhibit the evolution process of dome height in the three stages that verify the correctness and accuracy of the mixed finite element model presented in this paper. A simply supported rectangular THUNDER actuator is used to investigate the actuating capability under heavy load, the effect of piezothermoelastic coupling problems on actuating displacement, and the capability to reduce the effect caused by temperature variation.

A. Verifying the Accuracy of Shape and Dome Height

For a 25.4 mm × 25.4 mm square actuator, its material parameters taken from [2,3,5,22,24] are given in Table 1. In the cooling process, the curing temperature is 250°C, room temperature is 25°C. Simply, it is assumed that the cooling process is caused only by thermal convection. To save computational time, the thermal convection coefficient is assumed as $h_v = 10^4$ W/(m^2°C) in order to make the structure's temperatures decreasing rapidly and reaching stable state. In the repoling process and actuating process, the temperature is constant and equal to room temperature. The applied external voltage in the actuating process is $100\sin[2\pi(t-2)]$ V.

Figure 4 shows that the structure's temperatures decrease rapidly and reach stable state 25°C at about 0.3 s. The temperature of structure's surface declines faster than that of the inner midpoint, which is satisfied with the common rules for the special type of thermal boundary conditions.

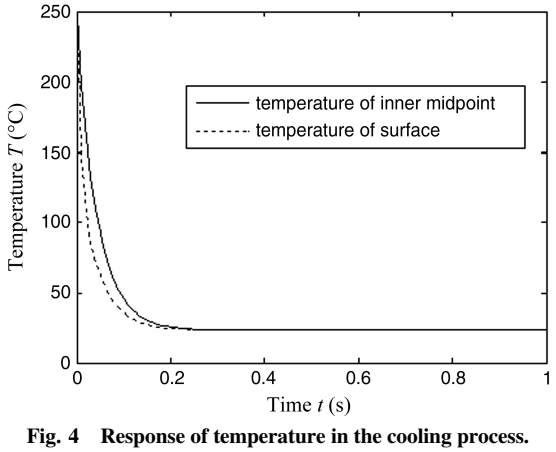

Fig. 4 Response of temperature in the cooling process.

Table 2 Dome height formed in the cooling process, $\Delta T = -225°C$

Result	Dome height, 10^{-3} m	Relative error
NASTRAN result [2]	1.0160	——
Dynamic result	1.0274	$(1.0274 - 1.0160)/1.0160 = 1.12\%$
Static result	0.9954	$(0.9924 - 1.0160)/1.0160 = -2.03\%$

For this example, Taleghani and Campbell [2] used a NASTRAN nonlinear finite element model to calculate the static dome height formed in the cooling process and measured the peak to peak displacements of dome height due to the voltage applied in experiments. However, the repoling process was not considered in their researches. For the repoling process, Capozzoli et al. [3] employed experimental methods to prove that the repolarization has a significant effect on dome height. As shown in their three experiments for three different actuators, the reduction percentages of dome height are 13.48, 15.93, and 27.32%, respectively. However, their experiments did not include the actuating process. Therefore, the results obtained by Taleghani and Campbell [2] are used as benchmark to directly test the accuracy of the results obtained in this paper for the cooling process and actuating process. In addition, the results given in [3] are used to indirectly verify the correctness of the model and method presented in this paper for the repoling process.

According to the mixed model, each material layer is divided into 256 rectangular parallelepiped elements with the same size and only one element is on each layer. The total degrees of freedom for displacement, temperature, and potential are 1280, 1536, and 2, respectively. According to [4–8], multiple equilibrium shapes exist for cooled THUNDER actuators in the case of a free–free boundary condition. For simplicity, the following boundary conditions are assumed in finite element dynamic analysis: namely, for the four vertices of square actuator, one vertex's displacements along the x axis, y axis, and z axis are constrained; one vertex's displacements along the y axis and z axis are constrained; and the other two vertices' displacements along the z axis are constrained. Assuming that the damping ratio is 0.3 and letting $\Delta t = 0.01$ s, the computational results of dome height formed in the cooling process, response of temperature in the cooling process, and full response of dome height in the three stages are given in Table 2 and Figs. 4 and 5, respectively.

In Table 2, the relative errors for the dome heights formed in the cooling process are also listed. It can be easily observed that both the static and dynamic methods presented in this paper have good accuracy for the cooling process.

Figure 5 shows the full dynamic response from the cooling process and repoling process to the actuating process. The reduction of dome height due to repolarization is 16.29%, from the point of variation trend and the order of magnitude, it satisfies with the research results in [3]. For the actuating process, the calculated result is very close to the experimental value presented in [2].

References [2,3] did not involve the curved shape of a THUNDER actuator. For shape prediction, Aimmanee and Hyer [7] used a 23-term Rayleigh–Ritz model to especially investigate the shape characteristics of rectangular THUNDER actuators with various side-length-to-thickness ratios when they are cooled from the adhesive curing temperature to room temperature. One of their examples, a square actuator of 85.4 by 85.4 mm, is chosen here to verify the paper's calculating accuracy on shape prediction. When its displacement fields are divided into 400 elements with the same size, the calculated results are shown in Fig. 6, in which Fig. 6a is the contour plot of shape; Fig. 6b is the 3-D graphics composed of 2000 contours; and the Lx, Ly, and Lz are length, width, and total thickness of the actuator, respectively. The calculated results agree with the results presented in [7].

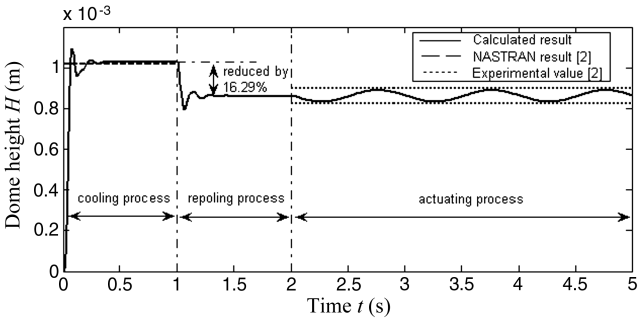

Fig. 5 Full response of dome height in the three stages.

B. Investigation of Piezothermoelastic Coupling Problem

As shown in Fig. 7, a 50.8×12.7 mm rectangular actuator is taken as the example to investigate the piezothermoelastic coupling problem. For the short edge AB, its displacements along the x axis and z axis are constrained, its thermal expansion along the y axis direction and rotation around the y axis are free; for the short edge CD, its displacement along the z axis are constrained, others are free. To constrain the rigid displacement along the y axis and considering the structure's symmetry, for the straight line connecting two midpoints of AB and CD, its displacements along the y axis are constrained. These displacement boundary conditions are used in the whole process from the cooling process and repoling process to the actuating process.

The actuator's material parameters are presented in Table 2. According to the mixed model presented above, each material layer is divided into 32×8 rectangular parallelepiped elements with the same size and an element on each layer. The total displacement freedom degree is 1280, temperature freedom degree is 1536, and potential freedom degree is 2. Discrete time Δt for dynamic analysis is 0.01 s. Similarly, the structure's curing temperature is assumed as 250°C, room temperature is 25°C, the thermal convection coefficient is 10^4 W/(m^2°C), and damping ratio is 0.01.

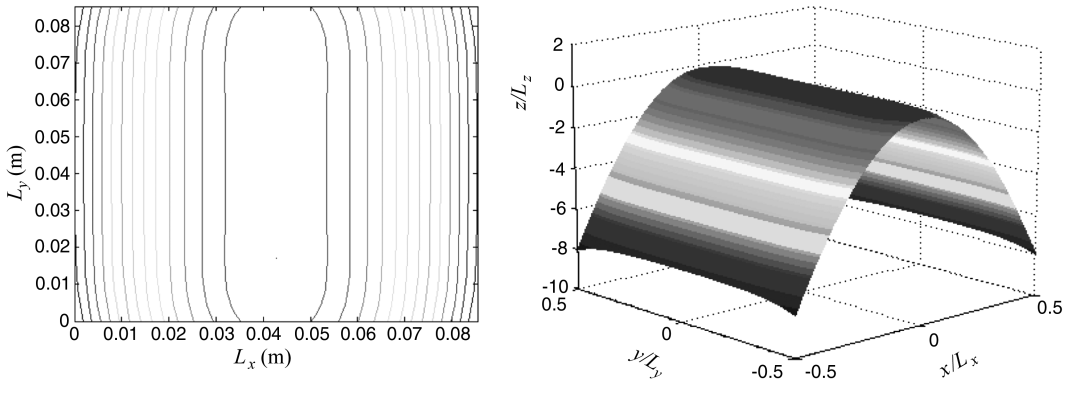

a) b)

Fig. 6 Room-temperature shape prediction: a) contour plot and b) 3-D graphics.

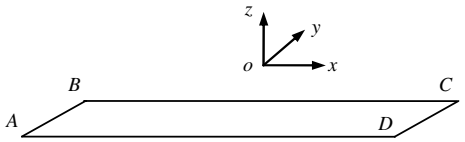

Fig. 7 A 50.8 × 12.7 mm rectangular actuator.

When the cooling process is finished, the room-temperature shape is shown in Fig. 8. The full dynamic response of dome height without load and temperature variation is shown in Fig. 9, in which the applied external voltage is assumed as $200\sin[2\pi(t-2)]$ V.

To investigate its actuating capability under various loads, the force applied at the actuator's midpoint along the positive direction of the z axis is varied from 0 to 15 N, and the step is 2.5 N. At the same time, the applied voltage is kept fixed at 400 V. The calculated results are presented in Fig. 10, from which it can be seen that the nonlinear relationship between actuating capability and loads is the concave curve. Relative to linear relation, the concave curve is beneficial in increasing its capacity in actuating displacement and bearing load.

To investigate the influence produced by temperature variation in the actuating process, a voltage of $100\sin(2\pi t)$ V is applied on the actuator and, at the same time, temperature rises 10°C. The calculated result of piezothermoelastic dynamics is shown as solid line in Fig. 11. To reflect the pyroelectric effect clearly, let pyroelectric constant $P_3 = 0$ and the calculated result is shown as dotted line in Fig. 11. The dash-dot line in Fig. 11 is the initial dome height. Compared with the initial position, the response curves move down, which is caused by thermal strain due to temperature rise. The difference between the solid line and the dotted line reflects the pyroelectric effect, which is determined by the pyroelectric constant P_3, temperature variation θ, and displacement fields $\boldsymbol{q}$. It can be seen from Fig. 11 that the thermal strain has a great effect on dome height and the pyroelectric effect has a relatively small but still noticeable effect on dome height.

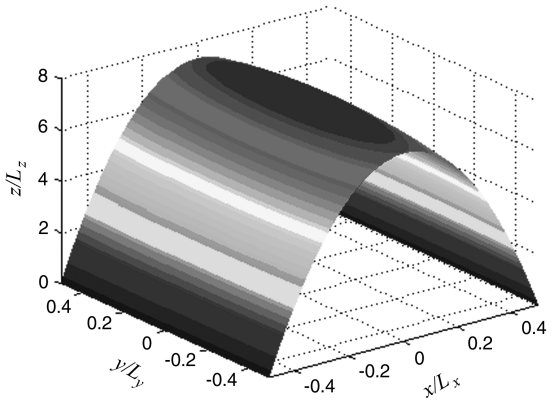

Fig. 8 Room-temperature shape.

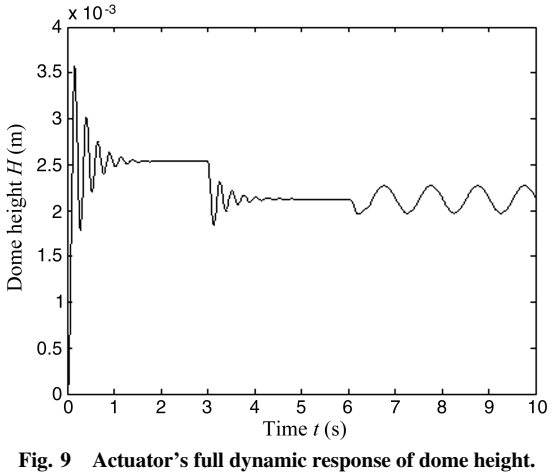

Fig. 9 Actuator's full dynamic response of dome height.

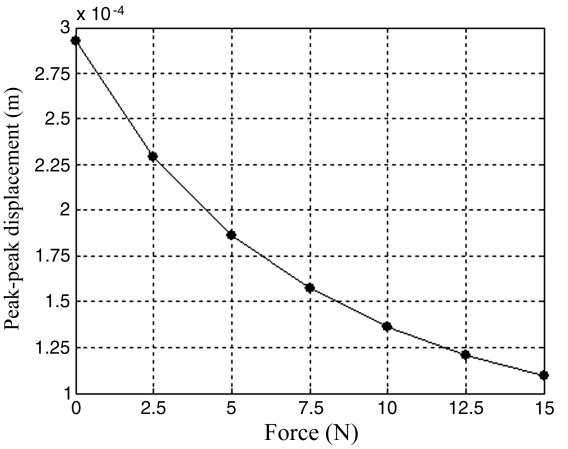

Fig. 10 Actuating displacement under various loads.

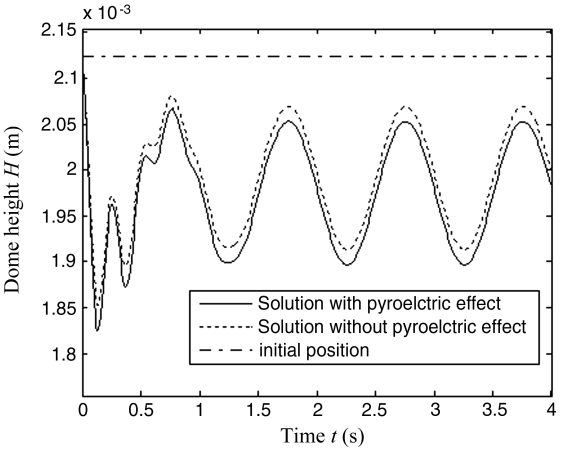

Fig. 11 Dome-height responses due to excitations.

Assuming the temperature variation is changed from −20 to 20°C, the step is 2.5°C, and at the same time, the applied voltage is kept fixed at 100 V, the relative errors of dome height due to neglecting pyroelectric effect are calculated as a solid line in Fig. 12, in which each dot corresponds to a temperature variation. Similarly, when the applied voltage is kept fixed at −100 V and others are the same, the relative errors are calculated as a dotted line in Fig. 12.

The following conclusions can be made from Fig. 12: the pyroelectric effect is related with voltage applied; for the two cases of

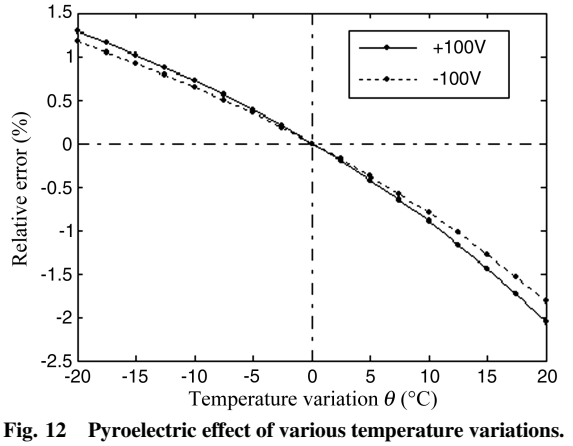

Fig. 12 Pyroelectric effect of various temperature variations.

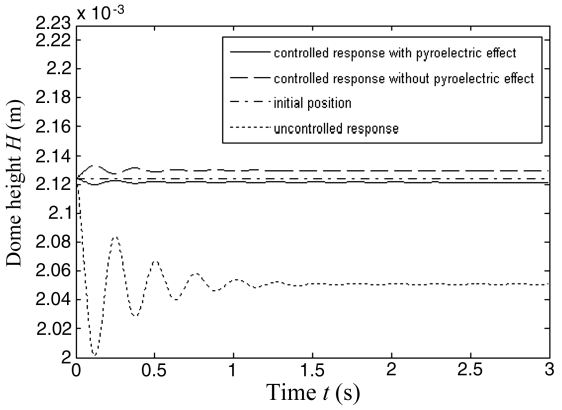

Fig. 13 Effects of control on temperature rise.

temperature rise and temperature decline, their pyroelectric effects are symmetry; and the nonlinear relation between pyroelectric effect and temperature variation is convex curve.

Although temperature variation has significant effect on THUNDER actuator's dome height, a THUNDER actuator itself has the ability to feel and reduce the effect. To investigate the ability, assuming environment temperature rises 10°C, the response of dome height without loads is calculated as the dotted line in Fig. 13. To reduce the effect of temperature variation, a voltage of −100 V is applied on the actuator, and the control effect is shown in Fig. 13.

It can be seen from Fig. 13 that the actuator has a good potential to reduce the influence caused by temperature variation, and the pyroelectric effect cannot be ignored in precise control.

V. Conclusions

The actuating capability of a THUNDER actuator is closely related with its manufacturing process, and the mechanical analysis of the three stages is beneficial in understanding its working mechanism. Simultaneously, since temperature variation is difficult to avoid in engineering applications, it is of great significance to study the piezothermoelastic coupling problems.

In this study, for THUNDER actuator's special structures, a mixed piezothermoelastic finite element model is presented. For the cooling process, repoling process, and actuating process, the dynamic behavior is studied and well correlated by the variable of initial displacement. The following conclusions can be drawn from the numerical results:

1) The mixed piezothermoelastic finite element model presented in this paper has good accuracy.

2) The nonlinear relationship between actuating capability and loads is a concave curve. Relative to linear relation, the concave curve is beneficial in increasing its capacity in actuating displacement and bearing load.

3) When temperature is varied in engineering application, thermal strain has a great effect and the pyroelectric effect has a relatively small but still noticeable effect on dome height; the pyroelectric effect is related with voltage applied; for the two case of temperature rise and temperature decline, their pyroelectric effects are asymmetric; the nonlinear relationship between pyroelectric effect and temperature variation is a convex curve.

4) Although temperature variation has a great effect on THUNDER actuator's dome height, a THUNDER actuator itself has a good ability to reduce the effect, in which the pyroelectric effect has an evident effect and cannot be ignored in precise control.

Appendix: Expressions of Symbols in Eqs. (21–23)

$$\boldsymbol{M}_{uu} = \int_{V_{\mathrm{AL}}+V_{\mathrm{SI}_1}+V_{\mathrm{PZT}}+V_{\mathrm{SI}_2}+V_{\mathrm{steel}}} \rho \boldsymbol{N}_u^T \boldsymbol{N}_u \ddot{\boldsymbol{q}}\, \mathrm{d}V$$

$$\boldsymbol{K}_{uu} = \int_{V_{\mathrm{AL}}+V_{\mathrm{SI}_1}+V_{\mathrm{PZT}}+V_{\mathrm{SI}_2}+V_{\mathrm{steel}}} \boldsymbol{B}_u^T \boldsymbol{S}^E \boldsymbol{B}_u\, \mathrm{d}V$$

$$\boldsymbol{K}_{uu}^{t0} = \int_{V_{\mathrm{AL}}+V_{\mathrm{SI}_1}+V_{\mathrm{PZT}}+V_{\mathrm{SI}_2}+V_{\mathrm{steel}}} \boldsymbol{B}_u^T \boldsymbol{S}^E \boldsymbol{B}_u^0\, \mathrm{d}V$$

$$\boldsymbol{B}_u^0 = (\boldsymbol{B}_L + \boldsymbol{B}_{\mathrm{non}})_{\boldsymbol{q}=\boldsymbol{q}_0}$$

$$\boldsymbol{K}_{u\Phi} = \int_{V_{\mathrm{PZT}}} \boldsymbol{B}_u^T \boldsymbol{e} \boldsymbol{B}_{\boldsymbol{\Phi}}\, \mathrm{d}V$$

$$\boldsymbol{K}_{q\theta} = \int_{V_{\mathrm{AL}}+V_{\mathrm{SI}_1}+V_{\mathrm{PZT}}+V_{\mathrm{SI}_2}+V_{\mathrm{steel}}} \boldsymbol{B}_u^T \boldsymbol{\lambda} \boldsymbol{N}_\theta\, \mathrm{d}V$$

$$\boldsymbol{F}_f = \int_{S_{\mathrm{top}}+S_{\mathrm{bottom}}} \boldsymbol{N}_u^T \boldsymbol{f}\, \mathrm{d}S$$

$$\boldsymbol{F}_{p_b} = \int_{V_{\mathrm{AL}}+V_{\mathrm{SI}_1}+V_{\mathrm{PZT}}+V_{\mathrm{SI}_2}+V_{\mathrm{steel}}} \boldsymbol{N}_u^T \boldsymbol{P}_b\, \mathrm{d}V$$

$$\boldsymbol{K}_{\Phi u} = \int_{V_{\mathrm{PZT}}} \boldsymbol{B}_{\boldsymbol{\Phi}}^T \boldsymbol{e}^T \boldsymbol{B}_u\, \mathrm{d}V$$

$$\boldsymbol{K}_{\Phi u}^{t0} = \int_{V_{\mathrm{PZT}}} \boldsymbol{B}_{\boldsymbol{\Phi}}^T \boldsymbol{e}^T \boldsymbol{B}_u^0\, \mathrm{d}V$$

$$\boldsymbol{K}_{\Phi\Phi} = \int_{V_{\mathrm{PZT}}} \boldsymbol{B}_{\boldsymbol{\Phi}}^T \boldsymbol{\varepsilon}^E \boldsymbol{B}_{\boldsymbol{\Phi}}\, \mathrm{d}V$$

$$\boldsymbol{K}_{\Phi\theta} = \int_{V_{\mathrm{PZT}}} \boldsymbol{B}_{\boldsymbol{\Phi}}^T \boldsymbol{P} \boldsymbol{N}_\theta\, \mathrm{d}V$$

$$\boldsymbol{F}_{\boldsymbol{\Phi}} = \int_{S_{\mathrm{PZT}}} (\xi_0 V_z / t_{\mathrm{PZT}})\, \mathrm{d}S$$

$$\boldsymbol{C}_{\theta u1} = T_0 \int_{V_{\mathrm{AL}}+V_{\mathrm{SI}_1}+V_{\mathrm{PZT}}+V_{\mathrm{SI}_2}+V_{\mathrm{steel}}} \boldsymbol{N}_\theta^T \boldsymbol{\lambda}^T \boldsymbol{B}_u\, \mathrm{d}V$$

$$\boldsymbol{C}_{\theta u2} = T_0 \int_{V_{\mathrm{AL}}+V_{\mathrm{SI}_1}+V_{\mathrm{PZT}}+V_{\mathrm{SI}_2}+V_{\mathrm{steel}}} \boldsymbol{N}_\theta^T \boldsymbol{\lambda}^T \dot{\boldsymbol{B}}_u\, \mathrm{d}V$$

$$\boldsymbol{C}_{\theta\Phi} = T_0 \int_{V_{\mathrm{PZT}}} \boldsymbol{N}_\theta^T \boldsymbol{P}^T \boldsymbol{B}_{\boldsymbol{\Phi}}\, \mathrm{d}V$$

$$\boldsymbol{C}_{\theta\theta} = T_0 \int_{V_{\mathrm{AL}}+V_{\mathrm{SI}_1}+V_{\mathrm{PZT}}+V_{\mathrm{SI}_2}+V_{\mathrm{steel}}} \boldsymbol{N}_\theta^T \boldsymbol{\alpha} \boldsymbol{N}_\theta\, \mathrm{d}V$$

$$\boldsymbol{K}_{\theta\theta} = \int_{V_{\mathrm{AL}}+V_{\mathrm{SI}_1}+V_{\mathrm{PZT}}+V_{\mathrm{SI}_2}+V_{\mathrm{steel}}} k \boldsymbol{B}_\theta^T \boldsymbol{B}_\theta\, \mathrm{d}V$$

$$\boldsymbol{K}_{\theta\theta_h} = \int_{S_{\mathrm{top}}+S_{\mathrm{bottom}}} h_v \boldsymbol{N}_\theta^T \boldsymbol{N}_\theta\, \mathrm{d}S$$

$$\boldsymbol{F}_{\theta_c} = \int_{S_{\mathrm{hc}}} (\boldsymbol{N}_\theta^T)_{S_{\mathrm{hc}}} \boldsymbol{q}_{\mathrm{heat}}\, \mathrm{d}S$$

$$\boldsymbol{F}_{\theta_h} = \int_{S_{\text{top}}} (\boldsymbol{N}_\theta^T)_{S_{\text{top}}} h_v (T_\infty - T_0)\, \mathrm{d}S + \int_{S_{\text{bottom}}} (\boldsymbol{N}_\theta^T)_{S_{\text{bottom}}} h_v (T_\infty - T_0)\, \mathrm{d}S$$

References

[1] Dogan, A., Tressler, J., and Newnham, R. E., "Solid-State Ceramic Actuator Designs," *AIAA Journal*, Vol. 39, No. 7, 2001, pp. 1354–1362. doi:10.2514/2.1454

[2] Taleghani, B. K., and Campbell, J. F., "Non-Linear Finite Element Modeling of THUNDER Piezoelectric Actuators," NASA TM-1999-209322, 1999.

[3] Capozzoli, M., Gopalakrishnan, J., Hogan, K., Massad, J., Tokarchik, T., et al., "Modeling Aspects Concerning THUNDER Actuators," *Proceedings of SPIE: The International Society for Optical Engineering*, Vol. 3667, March 1999, pp. 719–727.

[4] Campbell, J. F., "Quasi-Static Analysis of LaRC THUNDER Actuators," NASA TM-214872, 2007.

[5] Taleghani, B., "Validation of High Displacement Piezoelectric Actuator Finite Element Models," *Fifth European Conference on Smart Structure and Materials*, edited by P. F. Gobin, and C. M. Friend, Vol. 4073, 2000, pp. 37–45.

[6] Hyer, M. W., and Jilani, A., "Predicting the Deformation Characteristics of Rectangular Unsymmetrically Laminated Piezoelectric Materials," *Smart Materials and Structures*, Vol. 7, No. 6, 1998, pp. 784–791. doi:10.1088/0964-1726/7/6/006

[7] Aimmanee, S., and Hyer, M. W., "Analysis of the Manufactured Shape of Rectangular THUNDER-Type Actuators," *Smart Materials and Structures*, Vol. 13, No. 6, 2004, pp. 1389–1406. doi:10.1088/0964-1726/13/6/010

[8] Mossi, K., Mouhli, M., Simth, B. F., Mane, P. P., and Bryant, R. G., "Shape Modeling And Validation Of Stress-Biased Piezoelectric Actuators," *Smart Materials and Structures*, Vol. 15, No. 6, 2006, pp. 1785–1793. doi:10.1088/0964-1726/15/6/033

[9] Chung, S. W., and Kim, S. J., "Investigation of Actuating Displacement Performance of Curved Actuator by Large-Scale Computation," *Smart Materials and Structures*, Vol. 14, No. 4, 2005, pp. 615–623. doi:10.1088/0964-1726/14/4/020

[10] Mulling, J., Usher, T., Dessent, B., Palmer, J., Franzon, P., et al., "Load Characterization of High Displacement Piezoelectric Actuators with Various End Conditions," *Sensors and Actuators A (Physical)*, Vol. 94, Nos. 1–2, 2001, pp. 19–24. doi:10.1016/S0924-4247(01)00688-4

[11] Schwartz, R. W., and Narayanan, M., "Development of High Performance Stress-Biased Actuators Through the Incorporation of Mechanical Pre-Load," *Sensors and Actuators A (Physical)*, Vol. 101, No. 3, 2002, pp. 322–331. doi:10.1016/S0924-4247(02)00263-7

[12] Wise, S. A., "Displacement Properties of RAINBOW and THUNDER Piezoelectric Actuators," *Sensors and Actuators A (Physical)*, Vol. 69, No. 1, 1998, pp. 33–38. doi:10.1016/S0924-4247(97)01745-7

[13] Marouz, J. P., and Cheng, L., "A Feasibility Study of Active Vibration Isolation Using THUNDER Actuators," *Smart Materials and Structures*, Vol. 11, No. 6, 2002, pp. 854–862. doi:10.1088/0964-1726/11/6/305

[14] Gao, J. X., and Cheng, L., "Modelling of a High Performance Piezoelectric Actuator Assembly for Active and Passive Vibration Control," *Smart Materials and Structures*, Vol. 13, No. 2, 2004, pp. 384–392. doi:10.1088/0964-1726/13/2/017

[15] Rao, S. S., and Sunar, M., "Analysis of Distributed Thermopiezoelectric Sensors and Actuators in Advanced Intelligent Structure," *AIAA Journal*, Vol. 31, No. 7, 1993, pp. 1280–1286. doi:10.2514/3.11764

[16] Tzou, H. S., and Tseng, C. I., "Distributed Piezoelectric Sensor/Actuator Design Dynamic Measurement/Control Of Distributed Parameter Systems: A Piezoelectric Finite Element Approach," *Journal of Sound and Vibration*, Vol. 138, No. 1, 1990, pp. 17–34. doi:10.1016/0022-460X(90)90701-Z

[17] Tzou, H. S., and Ye, R., "Piezothermoelasticity and Precision Control of Piezoelectric Systems: Theory and Finite Element Analysis," *Journal of Vibration and Acoustics*, Vol. 116, No. 4, 1994, pp. 489–495. doi:10.1115/1.2930454

[18] Tzou, H. S., and Bao, Y., "A Theory on Anisotropic Piezothermoelastic Shell Laminates with Sensor/Actuator Applications," *Journal of Sound and Vibration*, Vol. 184, No. 3, 1995, pp. 453–473. doi:10.1006/jsvi.1995.0328

[19] Chattopadhyay, A., Li, J. M., Gu, H. Z., "Coupled Thermo-Piezoelectric-Mechanical Model for Smart Composite Laminates," *AIAA Journal*, Vol. 37, No. 12, 1999, pp. 1633–1638. doi:10.2514/2.645

[20] Gu, H. Z., Chattopadhyay, A., Li, J. M., and Zhou, X., "A Higher Order Temperature Theory for Coupled Thermopiezoelectric-Mechanical Modeling of Smart Composites," *International Journal of Solids and Structures*, Vol. 37, No. 44, 2000, pp. 6479–6497. doi:10.1016/S0020-7683(99)00283-8

[21] Zhou, X., Chattopadhyay, A., and Gu, H. Z., "Dynamic Response of Smart Composites Using a Coupled Thermo-Piezoelectric-Mechanical Model," *AIAA Journal*, Vol. 38, No. 10, 2000, pp. 1939–1948. doi:10.2514/2.848

[22] Lee, H. J., "Generalized Finite Element Formulation for Smart Multilayered Thermal Piezoelectric Composite Plates," *International Journal of Solids and Structures*, Vol. 34, No. 26, 1997, pp. 3355–3371. doi:10.1016/S0020-7683(96)00215-6

[23] Wang, D. W., "Dynamics and Distributed Control of Geometrically Nonlinear Active Piezothermoelastic Structronic Systems Using the Finite Element Technique," Ph.D. Dissertation, Univ. of Kentucky, 2003.

[24] Sharma, J. N., Pal, M., and Chand, D., "Three-Dimensional Vibration Analysis of a Piezothermoelastic Cylindrical Panel," *International Journal of Engineering Science*, Vol. 42, Nos. 15–16, 2004, pp. 1655–1673. doi:10.1016/j.ijengsci.2004.01.006

R. Kapania
Associate Editor